Journal of Power Sources 648 (2025) 237396

Contents lists available at ScienceDirect

Journal of Power Sources

journal homepage: www.elsevier.com/locate/jpowsour

Characterisation of mass transport in mesh-type flow-field based polymer electrolyte membrane water electrolysers by neutron imaging

Y. Wu [a,b,*], Y. Wen [b], I. Malone [b], A. Tengattini [c,d,e], L. Helfen [c], J. Johnstone-Hack [f], J. Majasan [b], Y. Li [a], Y. Han [a], Q. Li [a], W. Chen [a], A.J.E. Rettie [b,g], P.R. Shearing [h], D.J.L. Brett [i], R. Jervis [b,g,**]

[a] School of Electrical Engineering, Southwest Jiaotong University, Chengdu, Sichuan Province, 611756, China
[b] Electrochemical Innovation Lab (EIL), Department of Chemical Engineering, University College London, London, WC1E 7JE, United Kingdom
[c] Institut Laue-Langevin, 71 Avenue des Martyrs, Grenoble, Rhône-Alpes, 38042, France
[d] Univ. Grenoble Alpes, Grenoble INP, CNRS, 3SR, 1270 Rue de la Piscine, Grenoble, 38400, France
[e] Institut Universitaire de France (IUF), France
[f] School of Chemical, Materials and Biological Engineering, University of Sheffield, Sir Robert Hadfield Building, Mappin Street, Sheffield, S13JD, United Kingdom
[g] Advanced Propulsion Lab, University College London, London, E20 2AE, United Kingdom
[h] Engineering Science and ZERO Institute, Department of Engineering Science, University of Oxford, Parks Road, Oxfordshire, Oxford, OX1 3PJ, United Kingdom
[i] State Key Laboratory of Structural Chemistry, Fujian Institute of Research on the Structure of Matter, Chinese Academy of Sciences, Fuzhou, 350002, Fujian, China

HIGHLIGHTS

- Introduction of the mesh configuration as an innovative flow distributor in PEMWEs.
- *Operando* water distribution across the active area analysed via neutron radiography.
- Enhanced water distribution uniformity achieved with the mesh configuration.
- The mesh-type design delivers enhanced mass transport and improved performance.

GRAPHICAL ABSTRACT

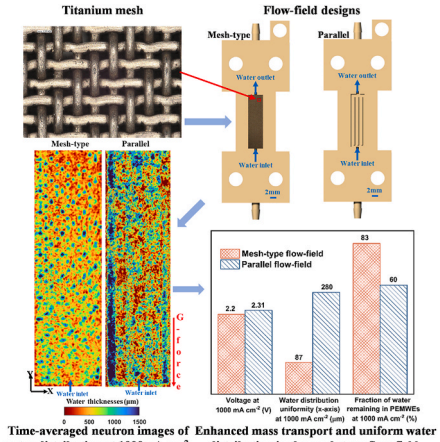

Time-averaged neutron images of water distribution at 1000mA cm^{-2}. Enhanced mass transport and uniform water distribution in the mesh-type flow-field.

ARTICLE INFO

Keywords:
Polymer electrolyte membrane water electrolysers

ABSTRACT

Flow-fields are essential for effective mass transport in polymer electrolyte membrane water electrolysers (PEMWEs). However, conventional flow-fields often face challenges in achieving reactant homogeneity across the full area of the electrode. This study explores the mass transport characteristics of PEMWEs using a mesh-type

* Corresponding author. School of Electrical Engineering, Southwest Jiaotong University, Chengdu, Sichuan Province 611756, China.
** Corresponding author.
E-mail addresses: wuyunsong@swjtu.edu.cn (Y. Wu), rhodri.jervis@ucl.ac.uk (R. Jervis).

https://doi.org/10.1016/j.jpowsour.2025.237396
Received 8 January 2025; Received in revised form 12 May 2025; Accepted 14 May 2025
Available online 21 May 2025

Mesh-type flow-field
Mass transport
Neutron imaging

flow-field, analysed through neutron imaging and electrochemical impedance spectroscopy. The mesh-type design demonstrates superior cell performance and lower mass transport resistance compared to the conventional parallel design under the conditions tested. Neutron imaging results show that the mesh-type flow-field achieves a more uniform water distribution across the active area, as indicated by significantly lower standard deviations in water thickness. In contrast, the parallel design experiences a more rapid decline in the fraction of water remaining in the flow-field area (indicating a significant build-up of gas bubbles and heterogeneity of available reactant water). This uniformity in water distribution, along with efficient gas transport, facilitates more effective electrochemical reactions, resulting in a ~5 % reduction in cell potential at a current density of 1000 mA cm^{-2} compared to the parallel design. These findings highlight the advantages of the mesh-type flow-field in addressing mass transport challenges, positioning it as a promising solution for a wide range of PEMWE applications.

1. Introduction

Polymer electrolyte membrane water electrolysers (PEMWEs) are considered one of the most promising devices for producing green hydrogen, characterized by fast start-up response time, high efficiency, high hydrogen purity, and cold-start capability [1–3]. However, obstacles persist in the wider adoption of this technology, including the mass transport limitations under high current densities [4]. For example, when the production of gas from water consumption surpasses the rate of water supply, the pores of the porous transport layer (PTL) become obstructed. These challenges significantly impede cell performance and longevity [5,6].

Flow-fields are crucial components of PEMWEs. Enhancing their design facilitates the removal of oxygen generated during electrolysis, diminishes mass transport resistance, and consequently improves cell performance [7–9]. These challenges become more pronounced in PEMWEs with larger active areas, and thus have practical relevance. Various flow-field designs have been proposed, among which parallel channels and serpentine designs are the most utilised [10–14]. These configurations rely on a series of channels for guiding the flow direction of the water to the catalyst layer through the PTL [15]. Despite their widespread use, the primary concern of these configurations is the uneven distribution of reactants as water is progressively consumed along the channels, resulting in worse performance [16,17].

One possible solution is to use a mesh-type flow-field [18]. A PEMWE featuring a mesh-type flow-field was employed and its electrochemical performance was compared to that of the conventional design with parallel channels (parallel design) [19]. Simulation results showed that the mesh-type design demonstrated increased current density, pressure, molar concentration of oxygen and hydrogen, along with a reduced temperature compared to the conventional parallel flow-field, which were attributed to the improved mass transport. A recent study proposed a Double-Layered Wire Mesh (DLWM) flow-field design and compared it numerically to the parallel and serpentine designs [20]. The PEMWE with DLWM design exhibited a higher local pressure drop and water velocity, which improved mass transport in the PTL and reduced concentration polarisation.

Experimental validation is necessary to confirm the validity of these numerical results. Additionally, the optimization of mesh-type flow-fields in PEMWEs lacks established design guidelines, and the mechanisms of mass transport through these structures are not well understood. Thorough investigations into these matters will aid in identifying existing design flaws and exploring alternative mesh microstructures to achieve improved performance [21].

A wide range of diagnostic techniques are employed in the field of PEMWEs. Optical visualisation, for example, is a widespread method for discerning liquid water movement within the flow channels [22–24]. However, this technique complicates the cell design because an observation window is needed for imaging, reducing its resemblance to a practical system. Electrochemical impedance spectroscopy (EIS) is commonly used to investigate various overpotential contributions to the overall performance of electrochemical devices due to its versatility and ease of application [25,26]. Several authors have employed this technique to reveal the effects of flow-field design [27], PTL microstructure [28] and catalyst loading [29] on the performance of PEMWEs. Although directly measuring water distribution inside PEMWEs using EIS is challenging, previous research has demonstrated that analysing EIS data obtained at high current densities can provide valuable insights into the mass transport properties of different PEMWE designs [30–32].

Neutron imaging is a powerful tool for examining *operando* water distribution and dynamics in both PEMWEs and polymer electrolyte membrane fuel cells (PEMFCs) [33–36]. The fundamental idea relies on the fact that neutron beams are strongly attenuated by liquid water but experience less attenuation as they pass through the various PEMWE components (such as the Ti/C PTLs and Ti/Al flow-fields). This difference arises because hydrogen atoms scatter neutrons significantly more than other common elements in water electrolysers because of the large neutron cross-section of hydrogen [37]. The mass transport properties of three commercial titanium fiber PTLs were evaluated using ex-situ neutron imaging by Altaf et al. [38]. The results showed that PTLs with larger fiber diameters and higher porosity improved mass transport. Additionally, using fibers with varying wettability was suggested to promote the formation of interfaces of zero curvature and enhance the efficiency of fluid transport. Maier et al. employed *operando* neutron imaging to compare the water distribution among three distinct PTLs during the PEMWE operation [39]. The study revealed significant variability in water distribution across the active area for the sinter and thick felt PTLs, highlighting the critical importance of PTL structure in reducing mass transport limitations at high current densities. The effects of temperature on the mass transport losses in PEMWE have also been investigated via neutron radiography by Lee et al. [40]. In contrast to the observed trends in overpotential due to mass transport, an increase in the quantity of oxygen gas at the anode was observed with higher temperatures. This divergence highlights a significant relationship between temperature variations and anode oxygen gas content. Using neutron imaging and a segmented sensor plate, the current density, temperature, and water distribution in PEMWEs with pin-type and parallel flow-fields were compared [41]. The results indicated that the pin-type design exhibited a more uniform distribution of current and temperature densities than its counterpart. However, the literature lacks comprehensive study into the mass transport in PEMWEs that employ mesh-type flow-fields. The investigation of mesh-type flow-fields is important as the findings can lead to materials and component optimization that can reduce cost and improve PEMWE performance [19].

This study employs an integrated experimental approach combining operando neutron imaging, EIS, and polarisation curve measurements to systematically quantify mass transport effects on PEMWE performance under mesh-type flow-field configurations. For comparative analysis between conventional channel-land structured design and the novel mesh-type design, parallel flow-field was implemented as the reference baseline. By integrating neutron imaging and EIS, water distribution within the electrolyser can be correlated with changes in impedance due to mass transport to identify the causes of the difference in mass transport between the two flow-field designs. This investigation establishes a foundational approach for analysing mass transport in PEMWEs using mesh-type flow-fields, essential for identifying current design

limitations.

2. Experimental setup

2.1. PEMWE design and test

Fig. 1 (a) depicts the assembly of the PEMWE, comprising anode and cathode plates made from gold-coated aluminium that integrates flow-fields, current collectors, and end plates. This 'mini cell' was designed for neutron radiography and future tomography experiments, and was adapted from previous PEMFC neutron cell designs [42,43]. Also shown are the catalyst-coated membrane (CCM), PTLs, and gaskets. Details on the configuration of the PEMWE are provided in Table 1. Fig. 1 (b) displays a simplified diagram of the experimental setup. Deionized water was supplied to both anode and cathode at an inflow temperature of 50 °C and a flow rate of 20 ml min^{-1} throughout the test. While PEMWE are typically operated between 60 and 80 °C, 50 °C was used here due to the long distance between the water bath heat exchanger and the PEMWE (limited by the neutron testing site). A Gamry Interface 5000 potentiostat was used for electrochemical measurements including polarisation curves and galvanostatic EIS measurements as well as for monitoring cell temperature using a Pt1000 sensor at the anode inlet. Polarisation curves were measured between 10 and 1000 mA cm^{-2} with a series of 60 s galvanostatic holds to ensure stability at each current density. The voltage measurements from the last 10 s of each galvanostatic hold were averaged to yield a single point on the polarisation curve.

EIS measurements were conducted using galvanostatic control. The PEMWE was operated under a constant current for 5 min prior to each impedance test to achieve steady-state conditions. The EIS tests were carried out at current densities of 500 and 1000 mA cm^{-2}, applying an AC modulation amplitude equivalent to 5 % of the DC input signal from 10 kHz to 0.1 Hz with 10 points per decade. Impedance data were presented using Nyquist plots, and parameters were extracted by fitting the experimental data to an equivalent circuit model using ZView (Scribner Associates, Inc.) software.

Table 1
PEMWE parameters.

Parameters	Value	Parameters	Value
Active area	19 mm × 5 mm	Compression torque	2.3 N m
CCM	Nafion® 115 membrane 0.4 mg cm^{-2} of platinum on the cathode side 1.7 mg cm^{-2} of iridium on the anode side (ITM Power, UK)	Mesh wire diameter	0.23 mm
PTL	Sintered titanium fibers(NIKKO Techno, Japan); Thickness:1 mm [39]	Mesh aperture	0.19 mm
		Mesh open area	20 %
		Land/channel width	0.7 mm
		Channel depth	1 mm

2.2. Flow-field design

This study utilised two symmetrical flow-field designs: parallel and mesh-type, as shown in Fig. 2(a and b). Deionized water was supplied to both anode and cathode via the inlets at the bottom of the cell. The performance of the parallel flow-field was selected as the baseline due to its moderate water velocity and pressure drop [41]. The configuration, consisting of four parallel channels, was machined into a 7.2 mm thick aluminium plate and coated with gold (Fig. 2 (a)). The value of channel/land width (as seen in Table 1) are designed to balance the water transport, thermal regulation and ohmic losses [13]. For the mesh-type flow-field configuration separate end plates with 19 × 5 mm rectangular machined compartments were used to house the mesh between the CCM and each end plate as illustrated in Fig. 1 (b). Fig. 2 (c) presents an optical microscopy image of the titanium mesh utilised in this study (Goodfellow, UK) which has a thickness of 0.75 mm. A highly compressible silicone gasket (2 mm thick) was used between each end plate and the CCM to ensure proper sealing and compression. Further

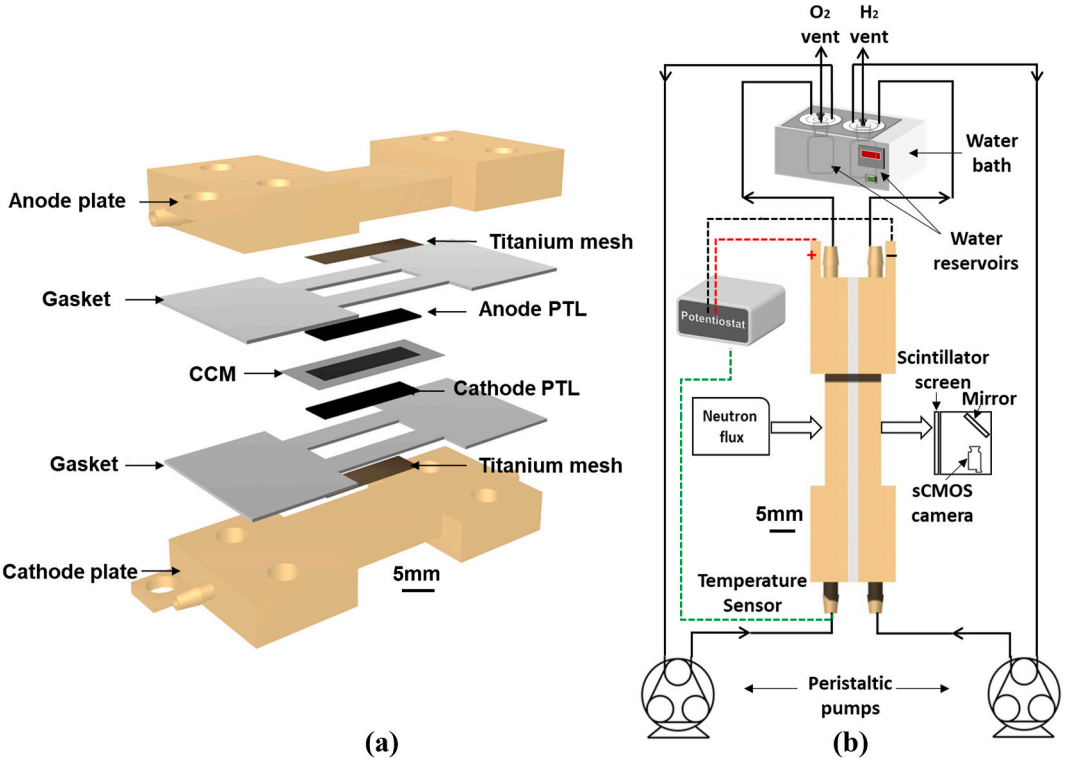

Fig. 1. (a) Exploded view of the PEMWE assembly and (b) Schematic of the experimental setup.

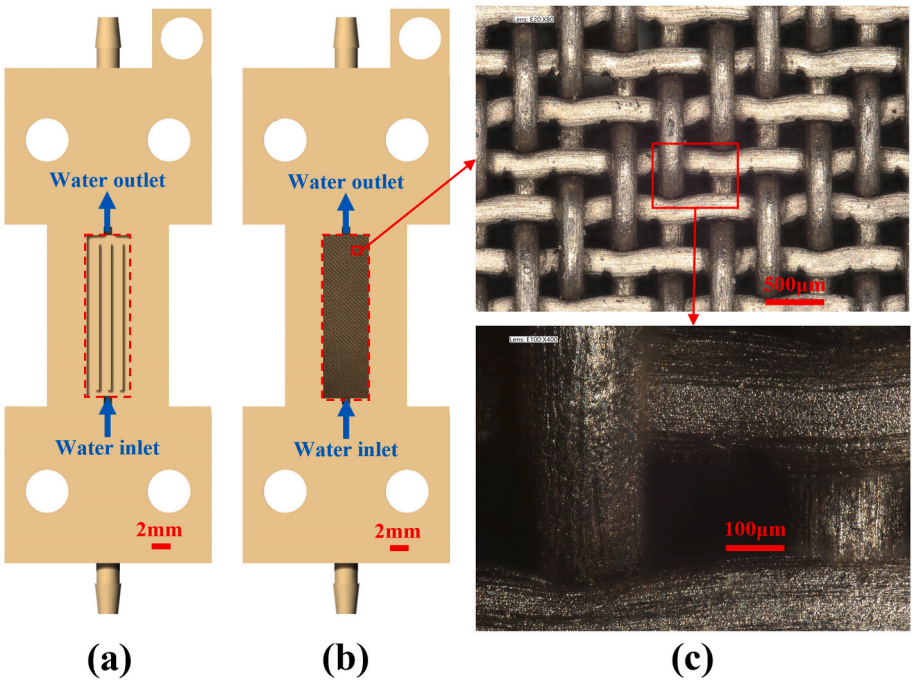

Fig. 2. Flow-field designs in this study: (a) Parallel design, (b) Mesh-type design, and (c) optical microscope images of the titanium mesh. The active areas have been highlighted by dashed red lines for clarity. (For interpretation of the references to colour in this figure legend, the reader is referred to the Web version of this article.)

details on the components and materials used are given in Table 1.

2.3. Neutron imaging

The experiment was conducted on the NeXT instrument at Institut Laue-Langevin (ILL) in Grenoble, France [44]. NeXT provides enhanced image contrast through its "cold" beam, with flux peaking at 2.8 Å, and a high neutron flux reaching 3×10^8 n cm^{-2} s^{-1} for an L/D ratio of 333 at the sample position [45]. A Hamamatsu ORCA sCMOS camera, featuring 2048 × 2048 pixels each 6.5 μm in size, was used as the detector and placed opposite a 20 μm thick Gadox scintillator screen. The PEMWE was oriented perpendicular to the beam, enabling comprehensive visualisation of liquid water distribution across the active area. Imaging utilised a demagnification ratio of 2.4, resulting in a field-of-view measuring 32 × 32 mm^2, and achieving a pixel resolution of 31 μm (with 2 × 2 pixel binning). Each radiography image was recorded with an exposure time of 2 s. Dark-field (captured without the neutron beam) and dry images (taken before water circulation through the PEMWE) were recorded prior to each electrochemical test for use in image processing and normalisation. The spatial distribution of water thickness across the active area was then quantified using the Beer-Lambert law [38,39]. All image processing was conducted with ImageJ.

Water remaining (R_{H_2O}) is defined as the averaged mass of liquid water within active area of the PEMWE under specified current density conditions, as expressed in Equation (1):

$$R_{H_2O} = \rho_{H_2O} \cdot \int_0^S T_{H_2O} . dS \tag{1}$$

where ρ_{H_2O} represents the water density, S denotes the active surface, and T_{H_2O} signifies the liquid water thickness at individual pixel coordinates, which was quantified using Beer-Lambert law [38,39].

3. Results and discussion

3.1. Overall performance comparison for two flow-field designs

To evaluate the overall performance of PEMWEs, the polarisation curves for both mesh and parallel flow-field designs are shown in Fig. 3 (a). The performance of both designs is relatively low compared to typical values in the literature (under 1.8 V at 2000 mA cm^{-2}) [4]. However, this outcome aligns with previous "mini cell" studies [46,47] and may result from the combined effects of an unrepresentative PEMWE design and the low temperature (50 °C) used in this study. Both designs exhibit a similar trend of increasing voltage with rising current density. This is typical behaviour in PEMWEs due to the activation, ohmic, and concentration overpotentials. At low current densities (up to 500 mA cm^{-2}), both flow-fields show comparable performance. However, beyond this point, the mesh-type design exhibits slightly lower voltages than the parallel design. At a current density of 1000 mA cm^{-2}, the overpotential of the parallel design is approximately 5 % higher than that of the mesh-type design, suggesting that the latter flow-field might be more efficient at higher current densities. The observed performance discrepancy across current density regimes is possibly due to the transition in dominant mass transport mechanisms [48]. Under lower current densities (<500 mA/cm^2), diffusion-governed transport prevails, where the mesh's intricate pore architecture prolongs effective diffusion lengths compared to parallel design. This extended path delays reactant delivery to catalytic interfaces. Conversely, at elevated current densities, the mesh structure tends to cause enhanced convection, which promotes higher water velocity and pressure drop [20], resulting in improved mass transport. To further investigate the root cause of the performance difference between the two flow-field designs, the amount of water remaining in PEMWEs was analysed as a function of current density [39,41]. Due to the differing void volumes in the two flow-field designs, the initial water content inside the PEMWE varies significantly in the 'initial state' where water is circulating but no electrochemical reaction occurs. The weight of liquid water in the PEMWE with the parallel flow-field is approximately 110 mg, compared to about 70 mg in the PEMWE with the mesh-type flow-field. Consequently, the fraction of water remaining

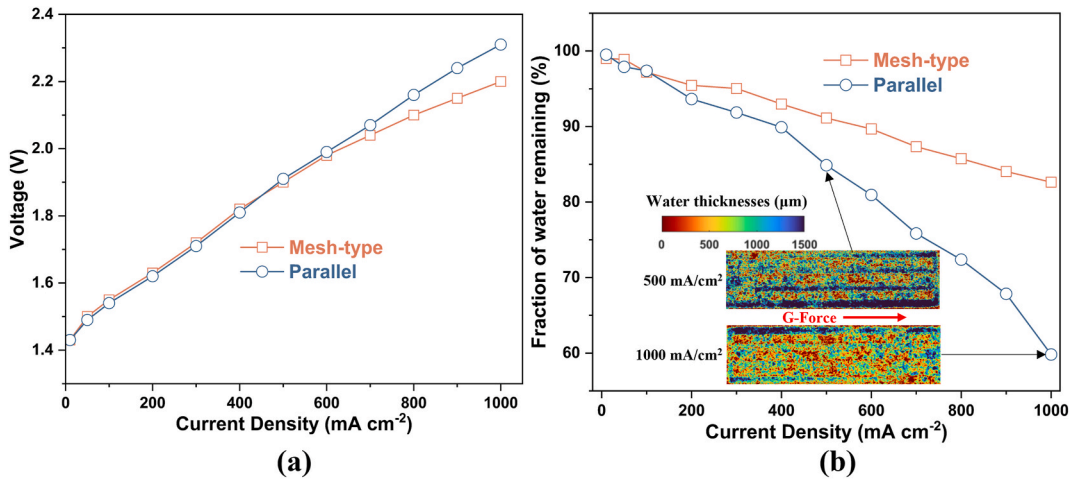

Fig. 3. (a) Polarisation curve and (b) fraction of water remaining of PEMWEs with mesh-type (squares) and parallel (circles) flow-field designs.

compared to their corresponding 'initial states' is employed in the current study.

Fig. 3 (b) shows the fraction of water remaining as a function of current density for both designs. As current density increases, the fraction of water remaining decreases for both designs. This is due to higher current densities leading to higher water consumption and increased gas generation. The parallel flow-field shows a rapid decline in the fraction of water remaining, as seen in the comparison of water

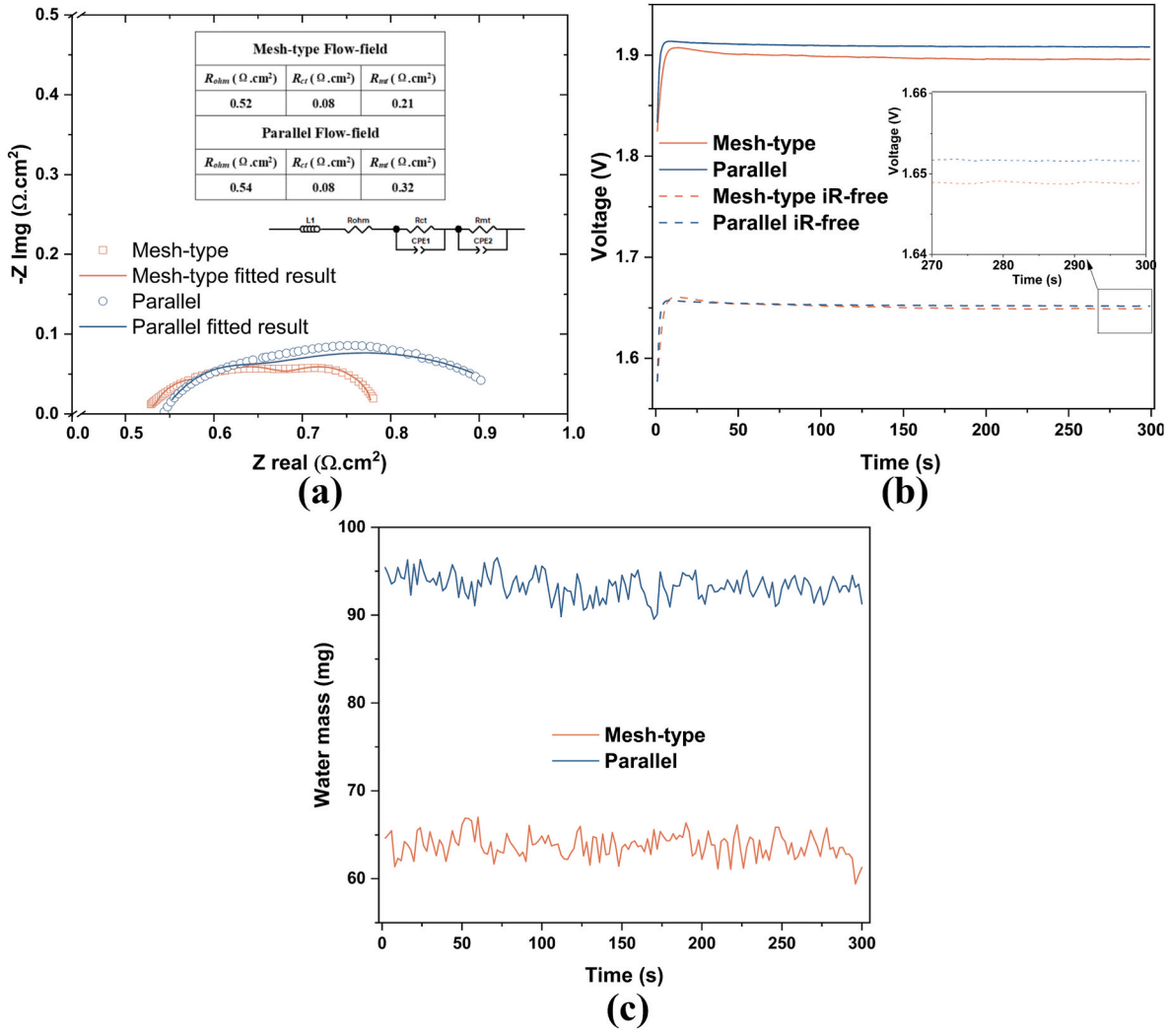

Fig. 4. (a) Nyquist plots of EIS spectra, as well as the evolution of (b) voltage and (c) water mass for mesh-type and parallel flow-field designs at a current density of 500 mA cm^{-2}. The equivalent circuit used to fit the EIS and results of the fitting (table) are shown in (a).

distribution, as shown inset in Fig. 3 (b). At low current densities (up to 500 mA cm^{-2}), the PEMWE with the mesh-type flow-field shows a slight increase in the fraction of water remaining compared to the parallel design, with a difference of less than 6 %. This difference becomes more pronounced at higher current densities. At 1000 mA cm^{-2}, the parallel design retains about 60 % of the water, while the mesh-type design retains approximately 83 %. This suggests that the mesh-type flow-field offers improved enhanced gas removal efficiency.

The analysis of the polarisation curve and the fraction of water remaining demonstrates that the mesh-type flow-field design offers superior performance in PEMWEs, particularly at higher current densities. This design provides lower overpotential and improved mass transport compared to the parallel flow-field design. Given the significant performance variations of PEMWEs with the two designs at medium and high current densities, a subsequent detailed analysis is conducted at two specific current densities in the following sections: 500 mA cm^{-2} and 1000 mA cm^{-2}.

3.2. Water distribution and performance of PEMWEs at 500 mA cm^{-2}

Electrochemical impedance spectroscopy (EIS) was employed to analyse the performance enhancement of the mesh-type flow-field design by separating different voltage losses at 500 mA cm^{-2}. The Ohmic resistance (R_{ohm}), charge transport resistance (R_{ct}) and mass transport resistance (R_{mt}) were determined by fitting the Nyquist plots to an equivalent circuit model established by Lin et al. [8]. The fitted results are shown in Fig. 4 (a), with the derived parameters listed in the included table. The R_{ct} of both flow-field designs is 0.08 Ω cm^2, which is mainly determined by catalyst layer properties and electrode architecture [4,49]. The mesh-type flow-field demonstrates a slightly lower R_{ohm} at 0.52 Ω cm^2 compared to the parallel flow-field (0.54 Ω cm^2). This improvement can be attributed to the improved contact between the mesh-type flow-field and the PTL [19]. Additionally, the R_{mt} is also lower for the mesh-type design (0.21 Ω cm^2) than for the parallel design (0.32 Ω cm^2). One possible explanation is that friction between the water and the mesh configuration leads to a higher local pressure drop and increased velocity [19]. This effect enhances gas removal in the flow field region, improving mass transport within the mesh-type flow-field design.

Fig. 4 (b) depicts the measured voltage and iR-free voltage (dash lines) evolution with time over 300 s for the mesh and parallel flow-field designs at a current density of 500 mA cm^{-2}. Initially, both designs exhibit a sharp increase in measured voltage due to the sudden increase in current. The cell equipped with the mesh-type flow-field quickly stabilizes at 1.90 V, 10 mV lower than the cell equipped with the parallel flow-field design at 1.91 V. The minor voltage variations observed between the two flow-field configurations can be attributed to their respective R_{ohm}, as evidenced by the negligible difference in iR-free data. The consistent voltage over the 300 s period for both designs suggests stable operation without performance fluctuations.

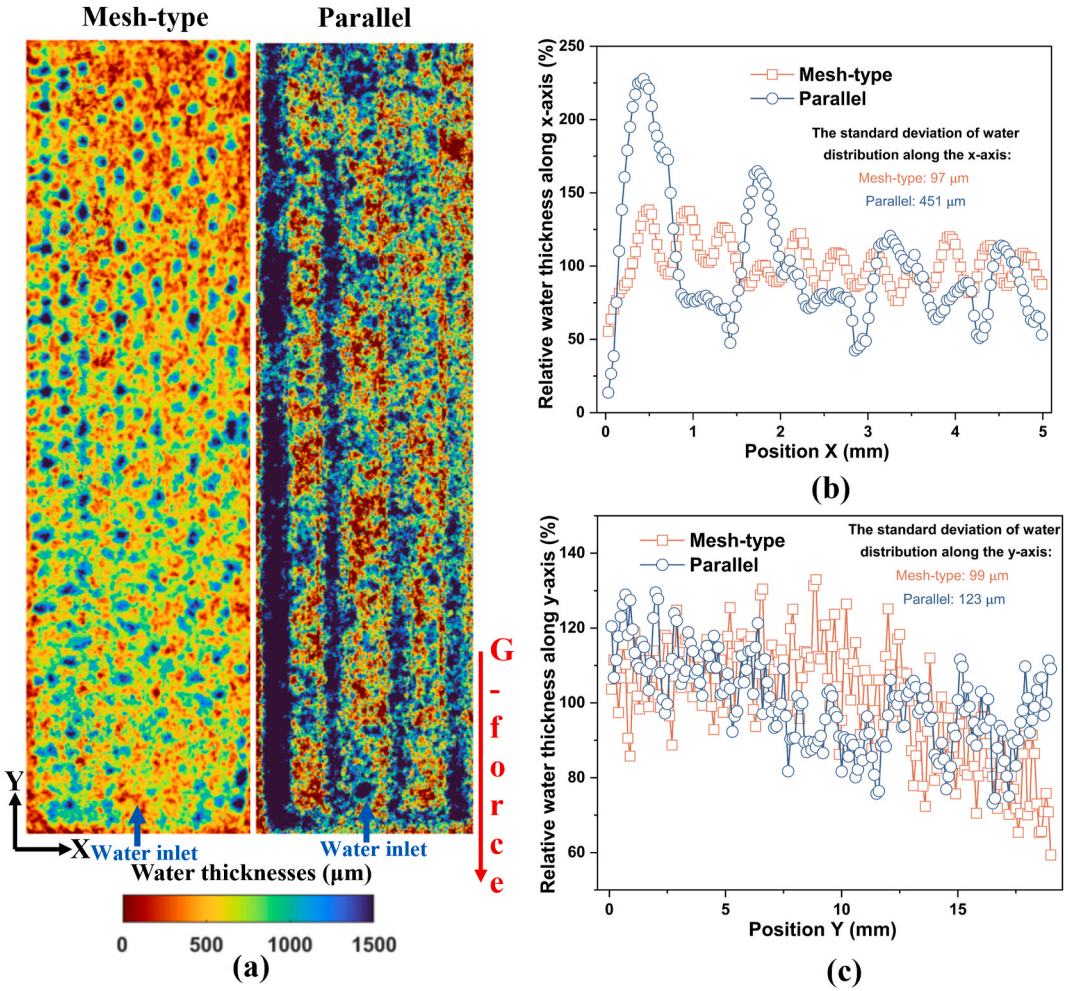

Fig. 5. (a) Time-averaged neutron images, relative water thickness along the x-axis (b) and y-axis (c) for mesh-type (red squares) and parallel flow-field (blue circles) designs at a current density of 500 mA cm^{-2}. (For interpretation of the references to colour in this figure legend, the reader is referred to the Web version of this article.)

Although EIS provides insights into the differences in mass transport capabilities among two flow-field designs, neutron imaging experiments offer a more direct method to determine if these variations stem from the water management effectiveness. Fig. 4 (c) illustrates the water mass in the PEMWE at a current density of 500 mA cm^{-2}. The water content within the PEMWE differs notably between the two designs due to variations in void volume. However, at this relatively low current density, both flow-field designs sustain a stable water mass over time, suggesting that mass transport limitations have not emerged at this stage for both designs [4].

Fig. 5 (a) presents the time-averaged neutron images for mesh-type and parallel flow-field designs at a current density of 500 mA cm^{-2}. Fig. 5 (a) illustrates significant differences in the liquid water thickness between PEMWEs utilising the two flow-field designs. To better highlight the details of liquid water thickness distribution in these designs, the upper limit of the colour bar for liquid water in Fig. 5 (a) is set to 1500 μm.

Fig. 5 (a) shows that a common characteristic of both designs is the accumulation of liquid water at the bottom of the PEMWEs. This accumulation results from the combined effects of gravity and the upward flow of water. Additionally, as bubbles rise toward the top of the PEMWE and gas escapes, the volume fraction of water decreases in this region. However, the mesh-type flow-field design demonstrates a more uniform water distribution, while the parallel flow-field design exhibits distinct channels with higher water density. This uniform distribution in the mesh-type design enhances the diffusion of reactants to the catalyst sites, promoting more efficient electrochemical reactions. In contrast, the parallel design exhibits more pronounced variations in water thickness, leading to uneven distribution and, subsequently, current density [41].

The heterogeneous distribution of water and current density has been demonstrated to induce localized thermal hotspots and accelerate degradation mechanisms, which can cause performance decline and shortened lifespan of PEMWEs [49,50]. Hence, it is crucial to assess the uniformity level of water thickness along both x-axis and y-axis. To achieve this, the time-averaged neutron images over the 300 s period (rather than a particular time) shown in Fig. 5 (a) are employed [33,51].

Since the initial water content inside the PEMWE varies significantly due to the differing void volumes in the two flow-field designs, the relative water thickness along the y-axis ($\%R_{H_2O\ (y)}$) is employed and defined as:

$$\%R_{H_2O\ (y)} = \frac{T_{H_2O\ (y_{Ave})}}{T_{H_2O\ (Ave)}}.100 \tag{2}$$

Where $T_{H_2O\ (Ave)}$ denotes the averaged thickness across the entire active area of corresponding flow-field design, $T_{H_2O\ (y_{Ave})}$ represents the averaged water thickness over the x-axis at each y position of corresponding flow-field design (coordinate system detailed in Fig. 5(a)), which is determined as follows:

$$T_{H_2O\ (y_{Ave})} = Ave\left(\int_{x=0}^{x_{max}} T_{H_2O(x,y)}.dx\right) \tag{3}$$

The relative water thickness along the x-axis ($\%R_{H_2O\ (x)}$) is defined as:

$$\%R_{H_2O\ (x)} = \frac{T_{H_2O(x_{Ave})}}{T_{H_2O\ (Ave)}}.100 \tag{4}$$

Where $T_{H_2O\ (x_{Ave})}$ represents the averaged water thickness over the y-axis at each x position of corresponding flow-field design (coordinate system detailed in Fig. 5(a)), which is determined as follows:

$$T_{H_2O\ (x_{Ave})} = Ave\left(\int_{y=0}^{y_{max}} T_{H_2O(x,y)}.dx\right) \tag{5}$$

The relative water thickness along both the *x*-axis ($\%R_{H_2O\ (x)}$) and *y*-axis ($\%R_{H_2O\ (y)}$) is illustrated in Fig. 5(b and c). The corresponding standard deviations of water thickness have also been calculated to quantify the variations.

Fig. 5 (b) reveals that both flow-field designs exhibit fluctuations in relative water thickness along the *x*-axis, indicating areas of varying water accumulation. However, the parallel flow-field design shows more significant peaks and valleys, reflecting greater variation in water thickness. This variability is partly attributed to viscous fingering effects amplified by continuous land interruptions [19,20]. Another possible explanation could be due to the inlet-induced momentum distortion through abrupt 90° flow reorientation. Both effects could contribute to the pronounced flow maldistribution in different channels of parallel designs. In contrast, the mesh-type flow-field demonstrates a significantly smaller standard deviation in water thickness (~97 μm) compared to the parallel design (~451 μm). These observations suggest that the mesh-type flow-field provides a more consistent water distribution across the x-axis, which is mainly attributed to the lack of a land/channel configuration.

Fig. 5 (c) illustrates the relative water thickness along the y-axis for the two different flow-field designs. The mesh configuration shows stable relative water thickness in the lower region ($y < 10$ mm), whereas a marked degradation occurs beyond this threshold ($y > 10$ mm). In contrast, the parallel design shows progressive decrease in relative water thickness along the y-axis, particularly beyond $y = 7.5$ mm. In addition to this, the mesh-type design demonstrates a relatively consistent water thickness, with a standard deviation of 99 μm. In contrast, the parallel flow-field design exhibits greater variability in water thickness along the y-axis, with a standard deviation of 123 μm.

3.3. Water distribution and performance of PEMWEs at 1000 mA cm^{-2}

Fig. 6 (a) presents the EIS testing results for both the mesh-type and parallel flow-field designs at a current density of 1000 mA cm^{-2}. Both flow field designs show minimal variation in R_{ct} compared to the 500 mA cm^{-2} condition, with the mesh design showing a slight reduction to 0.07 Ω cm^2, while the parallel design retains a value of 0.08 Ω cm^2. This observation aligns with previous findings documented in the literature [27], where activation-controlled nature at medium current densities are unchanged by variation in the cell design. Both designs show a slight reduction in Ohmic resistance (R_{ohm}) compared to the results at 500 mA cm^{-2}, due to the improved membrane conductivity at the higher current density [40]. The mesh-type design demonstrates a marginally lower R_{ohm} at 0.51 Ω cm^2 compared to the parallel design (0.52 Ω cm^2). The more notable difference is in the mass transport resistance (R_{mt}) where the mesh-type design exhibits an increase in R_{mt} at 0.25 Ω cm^2 compared to the results at 500 mA cm^{-2} (0.21 Ω cm^2), whereas the parallel flow-field shows an increase in R_{mt}, rising from 0.32 Ω cm^2 to 0.39 Ω cm^2. This demonstrates that the mesh-type flow-field effectively reduces mass transport limitations, in contrast to the parallel design becomes more mass transport limited.

The measured voltage and iR-free voltage (dash lines) evolution over time for both flow-field designs at a current density of 1000 mA cm^{-2} are presented in Fig. 6 (b). Initially, both designs exhibit a voltage drop, which stabilizes after a few seconds. The parallel flow-field maintains a higher stable voltage (~2.3 V) compared to the mesh-type design (~2.2 V). The distinct voltage discrepancy between the two designs at 1000 mA cm^{-2} is unlikely attributable to the R_{ohm}, but rather due to their divergent mass transport efficiencies, as evidenced by the iR-free voltage.

Fig. 6 (c) shows the evolution of water mass in the PEMWE during galvanostatic operation at 1000 mA cm^{-2}. Both designs show a decrease in water compared to their performance at 500 mA cm^{-2}, indicating an increase in accumulated gas at the higher current density, as expected. The mesh-type design exhibits a 10 % reduction in water mass, while the parallel design exhibits a 30 % decrease compared to results at 500 mA

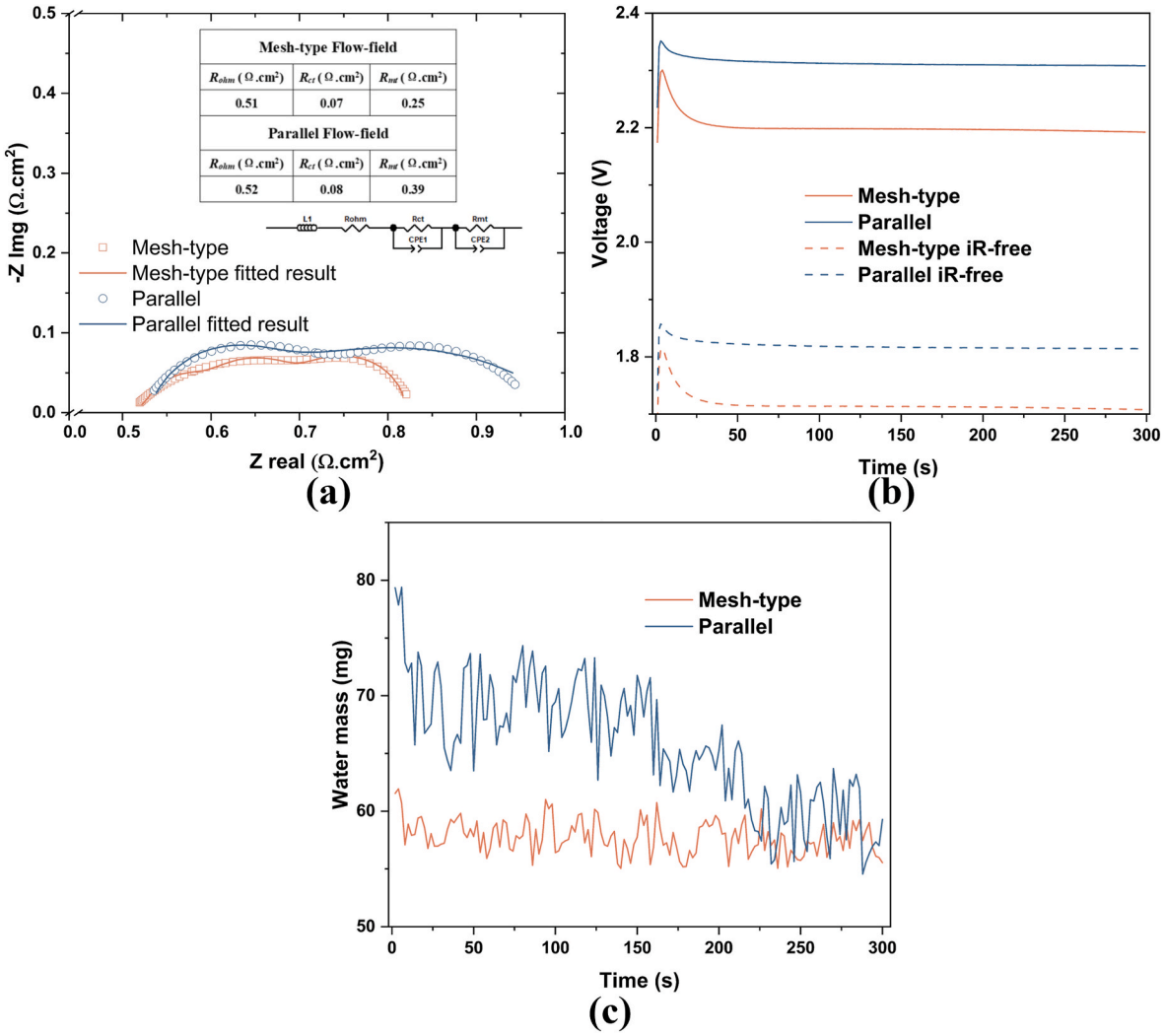

Fig. 6. (a) Nyquist plots of EIS spectra, as well as the evolution of (b) voltage and (c) water mass for mesh-type and parallel flow-field designs at a current density of 1000 mA cm^{-2}. The equivalent circuit used to fit the EIS and the results of the fitting (table) are shown in (a).

cm^{-2}, suggesting that the mesh-type design can handle the higher rate of gas production at higher current densities. Furthermore, the mesh-type design maintains a stable water mass of approximately 58 mg, demonstrating superior water management. In contrast, the parallel design, which starts with a higher initial water mass of approximately 70 mg due to differing void volumes, remains stable for the first 160 s. However, over the following 140 s, it rapidly declines to approximately 59 mg by the end of the measurement period, indicating reduced gas removal efficiency at higher current levels.

Fig. 7 (a) presents the time-averaged (over the 300 s period) neutron images for mesh-type and parallel flow-field designs at a current density of 1000 mA cm^{-2}. The neutron images illustrate an overall decrease in water content for both designs at higher current densities. In the parallel design, the water content exhibits a more pronounced decrease in the central region compared to that observed at 500 mA cm^{-2}, possibly due to the combined effects of inadequate gas removal and enhanced gas production rates at elevated current densities. In contrast, the mesh structure tends to cause local turbulence, which promotes higher water velocity and pressure drop [20], resulting in improved mass transport in the diffusion layer reducing concentration polarisation. This behavior is consistent with the observations at 500 mA cm^{-2}, as shown in Fig. 5 (a).

The relative water thickness along both the y-axis and x-axis are illustrated in Fig. 7(b and c). The corresponding standard deviations have also been calculated to quantify the variations. Fig. 7 (b) demonstrates that the water thickness in the mesh-type design remains relatively uniform along the *x*-axis, with only minor variations around the average. This stability is evidenced by a low standard deviation of around 87 μm, suggesting that the mesh-type flow-field maintains effective reactant distribution and water management even at higher current densities. At 1000 mA cm^{-2}, the parallel design shows a notable reduction in water thickness in the middle two channels (dashed black box) compared to 500 mA cm^{-2}. The standard deviation for the parallel design is approximately 280 μm, which is over three times greater than that of the mesh-type design, highlighting its less consistent water distribution.

Fig. 7 (c) depicts the relative water thickness along the *y*-axis for both designs. The mesh-type design demonstrates stable relative liquid water thickness distribution in the lower region ($y < 12$ mm), whereas a gradual decrease is observed beyond this threshold ($y > 12$ mm). In contrast, the parallel design exhibits significantly reduced relative water thickness in the middle region ($6\ mm < y < 12\ mm$). This aligns with the standard deviation data, where liquid water maintains a relatively uniform distribution in the mesh-type design, with a standard deviation of around 80 μm, compared to 99 μm at 500 mA cm^{-2}. In contrast, the parallel design shows a significant reduction in water thickness in the middle region compared to the top and bottom areas. This decreased water thickness highlights the limitations of the parallel flow-field's design, which can lead to less effective gas removal and uneven water

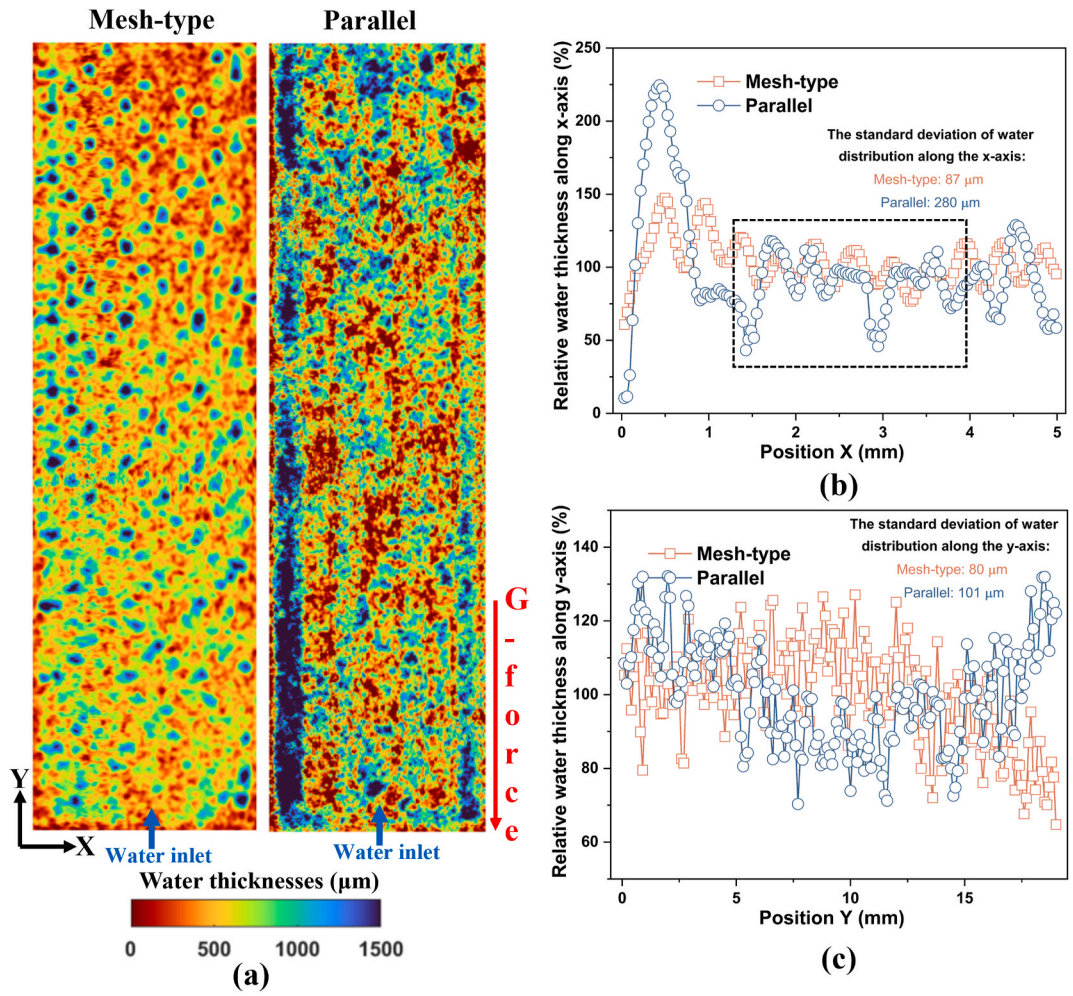

Fig. 7. (a) Time-averaged neutron images, relative water thickness along the x-axis (b) and y-axis (c) for mesh-type (red squares) and parallel flow-field (blue circles) designs at a current density of 1000 mA cm^{-2}. (For interpretation of the references to colour in this figure legend, the reader is referred to the Web version of this article.)

distribution. The parallel design exhibits a more variable water thickness along the *y*-axis, with a standard deviation of approximately 101 μm.

4. Conclusion

This study provides a detailed evaluation of the mesh-type flow-field as the flow distributor in polymer electrolyte membrane water electrolysers (PEMWEs), compared to the conventional parallel flow-field. Conducted under controlled conditions, the evaluation utilised neutron imaging, electrochemical impedance spectroscopy (EIS), and polarisation curves to investigate the mass transport characteristics and overall performance of both designs. The results highlight several significant advantages of the mesh-type design over its parallel counterpart, demonstrating its potential to enhance PEMWE performance.

1. The mesh-type design exhibited a highly uniform water distribution, with significantly lower standard deviations in water thickness (~97 μm) across the transverse direction (perpendicular to flow orientation) at a moderate current density of 500 mA cm^{-2}, compared to the parallel design (~451 μm). This uniformity, verified through neutron imaging, ensures consistent hydration levels throughout the cell, which is crucial for sustaining stable electrochemical reactions. In contrast, the parallel design displayed pronounced water channels and more variable water distribution.
2. The mesh-type design also showed superior mass transport characteristics. Detailed analysis using EIS revealed that the mesh-type flow-field exhibited significantly lower mass transport resistance (0.25 Ω cm^2) compared to the parallel design (0.39 Ω cm^2) at a higher current density of 1000 mA cm^{-2}. This improvement can be attributed to the higher local pressure drop and increased water velocity triggered by the friction between the water and the mesh configuration, thereby enhancing reactant delivery and gas removal. Consequently, the mesh-type design effectively addresses issues of reactant starvation and gas accumulation, which are particularly problematic in the parallel design under high operational current densities.
3. The structural advantages of the mesh-type design also translated into superior electrochemical performance. The uniform water distribution and efficient gas transport facilitated a more conducive environment for electrochemical reactions, resulting in a reduction in overpotential by approximately 5 % at a current density of 1000 mA cm^{-2} compared to the parallel design. This enhancement underscores the mesh-type design's ability to optimize the conditions for electrochemical processes.
4. Water management is a critical factor in the operation of PEMWEs. The study found that the mesh-type design effectively manages water within the cell, preventing issues like dry-out. In contrast, the parallel design limitations were evident in the observed rapid decline in water mass, especially under high operational current densities.

In summary, the mesh-type flow-field emerges as a superior design for PEMWEs, offering significant benefits in terms of uniform water distribution, enhanced mass transport, and improved performance. The results of this study also indicate that further refining the mesh-type flow-field, such as adjusting the aperture size and open area, could lead to additional performance improvements.

CRediT authorship contribution statement

Y. Wu: Writing – review & editing, Writing – original draft, Supervision, Methodology, Investigation, Funding acquisition, Formal analysis, Data curation, Conceptualization. **Y. Wen:** Writing – review & editing, Visualization, Methodology, Investigation, Formal analysis. **I. Malone:** Writing – review & editing, Visualization, Methodology, Investigation, Formal analysis. **A. Tengattini:** Resources, Methodology, Investigation. **L. Helfen:** Resources, Methodology, Conceptualization. **J. Johnstone-Hack:** Writing – review & editing, Methodology. **J. Majasan:** Writing – review & editing, Methodology. **Y. Li:** Writing – review & editing. **Y. Han:** Writing – review & editing. **Q. Li:** Writing – review & editing. **W. Chen:** Writing – review & editing. **A. Rettie:** Writing – review & editing, Formal analysis. **P.R. Shearing:** Writing – review & editing. **D.J.L. Brett:** Writing – review & editing, Supervision. **R. Jervis:** Writing – review & editing, Supervision, Project administration, Methodology, Funding acquisition, Conceptualization.

Declaration of competing interest

The authors declare that they have no known competing financial interests or personal relationships that could have appeared to influence the work reported in this paper.

Acknowledgements

Yunsong Wu gratefully acknowledges the financial support from National Natural Science Foundation of China (52307140), The Ministry of Education of China's Special Recruitment Program for Overseas Researchers, the Sichuan Province Tianfu Emei Young Talent Award, and an STFC Experimental Design Award (ST/R006873/1). The authors would also like to acknowledge the financial support from the EPSRC (EP/W033321/1, EP/S018204/2, EP/P009050/1 and EP/R023581/1) for supporting the Electrochemical Innovation Lab. The authors gratefully acknowledge ILL for the provision of beam time (2022-1-06-02). Iain Malone acknowledges the EPSRC and Johnson Matthey plc for funding through the Industrial Cooperative Awards in Science & Engineering (ICASE) scheme. Jennifer Johnstone-Hack acknowledges funding from The Royal Academy of Engineering under the Research Fellowship programme.

Appendix B. Supplementary data

Supplementary data to this article can be found online at https://doi.org/10.1016/j.jpowsour.2025.237396.

Data availability

Data will be made available on request.

References

[1] A. Bazarah, E.H. Majlan, T. Husaini, A. Zainoodin, I. Alshami, J. Goh, et al., Factors influencing the performance and durability of polymer electrolyte membrane water electrolyzer: a review, Int. J. Hydrogen Energy 47 (85) (2022) 35976–35989.
[2] B. Karthikeyan, G.P. Kumar, S. Basa, S. Sinha, S. Tyagi, P. Kamat, et al., Strategic optimization of large-scale solar PV parks with PEM Electrolyzer-based hydrogen production, storage, and transportation to minimize hydrogen delivery costs to cities, Appl. Energy 377 (2025) 124758.
[3] J. Chen, S. Wang, Y. Sun, C. Zhang, H. Lv, Multi-dimensional performance evaluation and energy analysis of proton exchange membrane water electrolyzer, Appl. Energy 377 (2025) 124457.
[4] M. Maier, K. Smith, J. Dodwell, G. Hinds, P.R. Shearing, D.J.L. Brett, Mass transport in PEM water electrolysers: a review, Int. J. Hydrogen Energy 47 (1) (2022) 30–56.
[5] Y.J. Kim, A. Lim, J.M. Kim, D. Lim, K.H. Chae, E.N. Cho, et al., Highly efficient oxygen evolution reaction via facile bubble transport realized by three-dimensionally stack-printed catalysts, Nat. Commun. 11 (1) (2020) 4921.
[6] H. Zhou, K. Meng, W. Chen, B. Chen, Exploratory research on bubbles migration behavior and mass transfer capacity evaluation of proton exchange membrane water electrolyzer based on a volume of fluid-coupled electrochemical model, Energy Convers. Manag. 290 (2023) 117217.
[7] L. Wu, Z. Pan, S. Yuan, X. Shi, Y. Liu, F. Liu, et al., A dual-layer flow field design capable of enhancing bubble self-pumping and its application in water electrolyzer, Chem. Eng. J. (2024) 151000.
[8] R. Lin, Y. Lu, J. Xu, J. Huo, X. Cai, Investigation on performance of proton exchange membrane electrolyzer with different flow field structures, Appl. Energy 326 (2022) 120011.
[9] D. He, K. Chen, W. Chen, Z. Luo, Z. Xiong, G. Zou, et al., Experimental study on the degradation of proton exchange membrane water electrolyzers under different dynamic loads and flow field configurations, J. Power Sources 641 (2025) 236844.
[10] A.H. Hassan, Z. Liao, K. Wang, F. Xiao, C. Xu, M.M. Abdelsamie, Characteristics of different flow patterns for proton exchange membrane water electrolysis with circular geometry, Int. J. Hydrogen Energy 49 (2024) 1060–1078.
[11] X. Luo, C. Ren, J. Song, H. Luo, K. Xiao, D. Zhang, et al., Design and fabrication of bipolar plates for PEM water electrolyser, J. Mater. Sci. Technol. 146 (2023) 19–41.
[12] L. Fan, Z. Tu, S.H. Chan, Recent development of hydrogen and fuel cell technologies: a review, Energy Rep. 7 (2021) 8421–8446.
[13] Z. Zhang, X. Xing, Simulation and experiment of heat and mass transfer in a proton exchange membrane electrolysis cell, Int. J. Hydrogen Energy 45 (39) (2020) 20184–20193.
[14] G. Li, L. Wu, Y. Qin, X. Du, G. Liu, Gradient catalyst layer design towards current density homogenization in PEM water electrolyzer with serpentine flow field, Energy Convers. Manag. 314 (2024) 118659.
[15] J. Zhang, X. Luo, Y. Ding, L. Chang, C. Dong, Effect of bipolar-plates design on corrosion, mass and heat transfer in proton-exchange membrane fuel cells and water electrolyzers: a review, Int. J. Miner. Metall. Mater. 31 (7) (2024) 1599–1616.
[16] R. Yang, J. Yesuraj, K. Kim, Effect of flow channel shape and operating temperature on the performance of a proton exchange membrane electrolyzer cell, Energy Fuels 37 (16) (2023) 12178–12191.
[17] B. Kimmel, D. Garcia-Sanchez, T. Morawietz, M. Schulze, I. Biswas, A. Gago, et al., Opportunities of in situ diagnostics and current distribution in proton exchange membrane water electrolyzers with segmented bipolar plates, Appl. Energy 380 (2025) 125106.
[18] A. Tugirumubano, K.S. Kim, H.J. Shin, C.H. Kim, L.K. Kwac, H.G. Kim, The design and performance study of polymer electrolyte membrane using 3-D mesh, Key Eng. Mater. 737 (2017) 393–397.
[19] Q. Wei, L. Fan, Z. Tu, Hydrogen production in a proton exchange membrane electrolysis cell (PEMEC) with titanium meshes as flow distributors, Int. J. Hydrogen Energy 48 (93) (2023) 36271–36285.
[20] P.R. Tirumalasetti, F.-B. Weng, M.M. Dlamini, G.-B. Jung, J.-W. Yu, C.C. Hung, et al., A comparative numerical analysis of proton exchange membrane water electrolyzer using different flow field dynamics, Int. J. Hydrogen Energy 65 (2024) 572–581.
[21] Y. Wu, X. Lu, J.I.S. Cho, L. Rasha, M. Whiteley, T.P. Neville, et al., Multi-length scale characterization of compression on metal foam flow-field based fuel cells using X-ray computed tomography and neutron radiography, Energy Convers. Manag. 230 (2021).
[22] M. Maier, Q. Meyer, J. Majasan, C. Tan, I. Dedigama, J. Robinson, et al., Operando flow regime diagnosis using acoustic emission in a polymer electrolyte membrane water electrolyser, J. Power Sources 424 (2019) 138–149.
[23] Y. Li, G. Yang, S. Yu, Z. Kang, D.A. Talley, F.-Y. Zhang, Direct thermal visualization of micro-scale hydrogen evolution reactions in proton exchange membrane electrolyzer cells, Energy Convers. Manag. 199 (2019) 111935.
[24] J. Mo, Z. Kang, S.T. Retterer, D.A. Cullen, T.J. Toops, Jr J.B. Green, et al., Discovery of true electrochemical reactions for ultrahigh catalyst mass activity in water splitting, Sci. Adv. 2 (11) (2016) e1600690.
[25] Y. Wu, L. Xu, S. Zhou, J. Yang, W. Kockelmann, Y. Han, et al., Water management and mass transport of a fractal metal foam flow-field based polymer electrolyte fuel cell using operando neutron imaging, Appl. Energy 364 (2024).
[26] A.J. McLeod, L.V. Bühre, B. Bensmann, O.E. Herrera, W. Mérida, Anode and cathode overpotentials under accelerated stress testing of a PEM electrolysis cell, J. Power Sources 589 (2024) 233750.
[27] J.O. Majasan, J.I. Cho, M. Maier, I. Dedigama, P.R. Shearing, D.J. Brett, Effect of anode flow channel depth on the performance of polymer electrolyte membrane water electrolyser, ECS Trans. 85 (13) (2018) 1593.
[28] Z. Kang, J. Mo, G. Yang, S.T. Retterer, D.A. Cullen, T.J. Toops, et al., Investigation of thin/well-tunable liquid/gas diffusion layers exhibiting superior multifunctional performance in low-temperature electrolytic water splitting, Energy Environ. Sci. 10 (1) (2017) 166–175.
[29] M. Bernt, A. Siebel, H.A. Gasteiger, Analysis of voltage losses in PEM water electrolyzers with low platinum group metal loadings, J. Electrochem. Soc. 165 (5) (2018) F305–F314.

[30] Q. Wang, Z. Zhou, K. Ye, M. Hu, X. Hu, S. Wang, et al., The effect of pretreatment and surface modification of porous transport layer (PTL) on the performance of proton exchange membrane water electrolyzer, Int. J. Hydrogen Energy 53 (2024) 163–172.
[31] J.C. Garcia-Navarro, M. Schulze, K.A. Friedrich, Measuring and modeling mass transport losses in proton exchange membrane water electrolyzers using electrochemical impedance spectroscopy, J. Power Sources 431 (2019) 189–204.
[32] P. Lettenmeier, R. Wang, R. Abouatallah, S. Helmly, T. Morawietz, R. Hiesgen, et al., Durable membrane electrode assemblies for proton exchange membrane electrolyzer systems operating at high current densities, Electrochim. Acta 210 (2016) 502–511.
[33] Y. Wu, J.I.S. Cho, T.P. Neville, Q. Meyer, R. Ziesche, P. Boillat, et al., Effect of serpentine flow-field design on the water management of polymer electrolyte fuel cells: an in-operando neutron radiography study, J. Power Sources 399 (2018) 254–263.
[34] Y. Wu, J.I.S. Cho, X. Lu, L. Rasha, T.P. Neville, J. Millichamp, et al., Effect of compression on the water management of polymer electrolyte fuel cells: an in-operando neutron radiography study, J. Power Sources 412 (2019) 597–605.
[35] S. Zhou, Y. Wu, L. Xu, W. Kockelmann, L. Rasha, W. Du, et al., Water content estimation in polymer electrolyte fuel cells using synchronous electrochemical impedance spectroscopy and neutron imaging, Cell Rep. Phys. Sci. 5 (9) (2024) 102208.
[36] Y. Wu, Q. Meyer, F. Liu, L. Rasha, J.I.S. Cho, T.P. Neville, et al., Investigation of water generation and accumulation in polymer electrolyte fuel cells using hydro-electrochemical impedance imaging, J. Power Sources 414 (2019) 272–277.
[37] P. Boillat, E.H. Lehmann, P. Trtik, M. Cochet, Neutron imaging of fuel cells – recent trends and future prospects, Curr. Opin. Electrochem. 5 (1) (2017) 3–10.
[38] H. Altaf, T. Milicic, T. Vidakovic-Koch, E. Tsotsas, A. Tengattini, N. Kardjilov, et al., Neutron imaging experiments to study mass transport in commercial titanium felt porous transport layers, J. Electrochem. Soc. 170 (6) (2023).
[39] M. Maier, J. Dodwell, R. Ziesche, C. Tan, T. Heenan, J. Majasan, et al., Mass transport in polymer electrolyte membrane water electrolyser liquid-gas diffusion layers: a combined neutron imaging and X-ray computed tomography study, J. Power Sources 455 (2020).
[40] C. Lee, J.K. Lee, M.G. George, K.F. Fahy, J.M. LaManna, E. Baltic, et al., Reconciling temperature-dependent factors affecting mass transport losses in polymer electrolyte membrane electrolyzers, Energy Convers. Manag. 213 (2020).
[41] C. Minnaar, F. De Beer, D. Bessarabov, Current density distribution of electrolyzer flow fields: in situ current mapping and neutron radiography, Energy Fuels 34 (1) (2019) 1014–1023.
[42] J. Hack, R.F. Ziesche, M. Fransson, T. Suter, L. Helfen, C. Couture, et al., Understanding water dynamics in operating fuel cells by operando neutron tomography: investigation of different flow field designs, J. Phys.: Energy 6 (2) (2024) 25021.
[43] R.F. Ziesche, J. Hack, L. Rasha, M. Maier, C. Tan, T.M.M. Heenan, et al., High-speed 4D neutron computed tomography for quantifying water dynamics in polymer electrolyte fuel cells, Nat. Commun. 13 (1) (2022) 1616.
[44] C. Tötzke, N. Kardjilov, N. Lenoir, I. Manke, S.E. Oswald, A. Tengattini, What comes NeXT?–High-Speed neutron tomography at ILL, Opt. Express 27 (20) (2019) 28640–28648.
[45] A. Tengattini, N. Lenoir, E. Andò, B. Giroud, D. Atkins, J. Beaucour, et al., NeXT-Grenoble, the neutron and X-ray tomograph in grenoble, Nucl. Instrum. Methods Phys. Res. Sect. A Accel. Spectrom. Detect. Assoc. Equip. 968 (2020) 163939.
[46] E. Leonard, A.D. Shum, S. Normile, D.C. Sabarirajan, D.G. Yared, X. Xiao, et al., Operando X-ray tomography and sub-second radiography for characterizing transport in polymer electrolyte membrane electrolyzer, Electrochim. Acta 276 (2018) 424–433.
[47] M.A. Hoeh, T. Arlt, I. Manke, J. Banhart, D.L. Fritz, W. Maier, et al., In operando synchrotron X-ray radiography studies of polymer electrolyte membrane water electrolyzers, Electrochem. Commun. 55 (2015) 55–59.
[48] W. Lee, I. Pyun, Y. Na, Concentric circular flow field to improve mass transport in large-scale proton exchange membrane water electrolysis cells, Energy Rep. 12 (2024) 3645–3653.
[49] C. Immerz, B. Bensmann, P. Trinke, M. Suermann, R. Hanke-Rauschenbach, Local current density and electrochemical impedance measurements within 50 Cm single-channel PEM electrolysis cell, J. Electrochem. Soc. 165 (16) (2018) F1292–F1299.
[50] B. Verdin, F. Fouda-Onana, S. Germe, G. Serre, P. Jacques, P. Millet, Operando current mapping on PEM water electrolysis cells. Influence of mechanical stress, Int. J. Hydrogen Energy 42 (41) (2017) 25848–25859.
[51] Y. Wu, J.I.S. Cho, M. Whiteley, L. Rasha, T.P. Neville, R. Ziesche, et al., Characterization of water management in metal foam flow-field based polymer electrolyte fuel cells using in-operando neutron radiography, Int. J. Hydrogen Energy 45 (3) (2020) 2195–2205.